ACS APPLIED MATERIALS & INTERFACES

Research Article

www.acsami.org

Iron Oxide-Induced Thermal Effects on Solid-State Upconversion Emissions in $NaYF_4$:Yb,Er Nanocrystals

Michael Challenor,[†,‡] Peijun Gong,[§] Dirk Lorenser,[§] Melinda Fitzgerald,[‡] Sarah Dunlop,[‡] David D. Sampson,[§,∥] and K. Swaminathan Iyer*[,†]

[†]School of Chemistry and Biochemistry, The University of Western Australia, 35 Stirling Highway, Crawley 6009, Australia

[‡]Experimental and Regenerative Neurosciences, School of Animal Biology, The University of Western Australia, 35 Stirling Highway, Crawley 6009, Australia

[§]Optical+Biomedical Engineering Laboratory, School of Electrical, Electronic and Computer Engineering, The University of Western Australia, 35 Stirling Highway, Crawley 6009, Australia

[∥]Centre for Microscopy, Characterisation & Analysis, The University of Western Australia, 35 Stirling Highway, Crawley 6009, Australia

Supporting Information

ABSTRACT: Multifunctional materials exhibiting photon upconversion show promising applications for biological imaging and sensing. In this study, we examine the solid-state upconversion emission of $NaYF_4$:Yb,Er nanoparticles in the presence of iron oxide nanoparticles. Fe_3O_4 nanoparticles (6 nm) were mixed with $NaYF_4$:Yb,Er nanoparticles (either 10 or 50 nm) in varying proportions by drying chloroform solutions of nanoparticles onto glass slides. Upconversion spectra were acquired, and a laser power-dependent emission was observed and correlated with the iron oxide content in the mixture. Changes in the lattice temperature of the upconverting particles were monitored by careful observation of the relative intensities of the $^2H_{11/2}$ and $^4S_{3/2} \rightarrow {}^4I_{15/2}$ transitions. The emission characteristics observed are consistent with an iron oxide-induced thermal effect that is dependent on both the laser power and the proportion of iron oxide. The results highlight that the thermal effects of mixed nanoparticle systems should be considered in the design of luminescent upconverting hybrid materials.

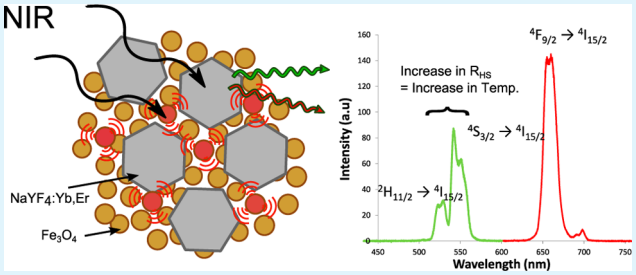

KEYWORDS: *upconversion, magnetite, quenching, nanoparticles, temperature, sensing*

INTRODUCTION

Upconversion nanoparticles are luminescent materials that convert near-infrared excitation into visible emission.[1] Upconversion nanocrystals exhibit sharp emission bands and large anti-Stokes shifts (up to 500 nm) that widely separate the emission peaks from the near-infrared (NIR) excitation.[2,3] The most efficient upconversion particles consist of a host lattice of $NaYF_4$, chosen for its low phonon lattice energy,[1] doped with Yb^{3+} sensitizers and Er^{3+} or Tm^{3+} emitters, which are responsible for the multiphoton excitation mechanism (Figure 1). The main erbium emissions are due to transitions to the ground state, $^4I_{15/2}$, from excited states $^4F_{7/2}$ (490 nm), $^2H_{11/2}$ (520 nm), $^4S_{3/2}$ (540 nm), and $^4F_{9/2}$ (650 nm). Upconversion has been shown to occur through three distinct mechanisms: energy-transfer upconversion (ETU), excited-state absorption (ESA), and photon avalanche (PA).[4,5] In Yb−Er codoped systems, ETU occurs when a ytterbium ion is excited from the ground state ($^2F_{7/2} \rightarrow {}^2F_{5/2}$) by a 980 nm photon and undergoes nonradiative decay via the transfer of energy of its excited state to a neighboring erbium ion within the lattice. The erbium ion undergoes a secondary excitation from a near-infrared photon, which promotes the electrons to the excited $^4F_{7/2}$ state ($^4I_{11/2} \rightarrow {}^4F_{7/2}$). Through multiphonon relaxation, the excited electrons populate the luminescent levels $^2H_{11/2}$ and $^4S_{3/2}$, giving rise to green emission. For red emission, the $^4F_{9/2}$ level must be populated either by further multiphonon relaxations from the $^2H_{11/2}$ and $^4S_{3/2}$ levels or through energy transfer from the ytterbium ion. The high sensitivity of the green $^2H_{11/2}$ and $^4S_{3/2} \rightarrow {}^4I_{15/2}$ transitions in the $NaYF_4$:Yb,Er system has been used to good effect in temperature sensors.[6−9] Because of the close proximity of these energy levels and the dependence of their differences on k_BT, where k_B is Boltzmann's constant and T is the absolute temperature (K), the relative peak intensities can be used to predict the lattice temperature of $NaYF_4$.

There has been considerable interest recently in the development of multifunctional nanoparticles to support multimodal imaging platforms.[10−12] One combination of imaging modalities under investigation is magnetic resonance imaging (MRI) and fluorescence microscopy, which combines

Received: May 15, 2013
Accepted: July 15, 2013
Published: July 15, 2013

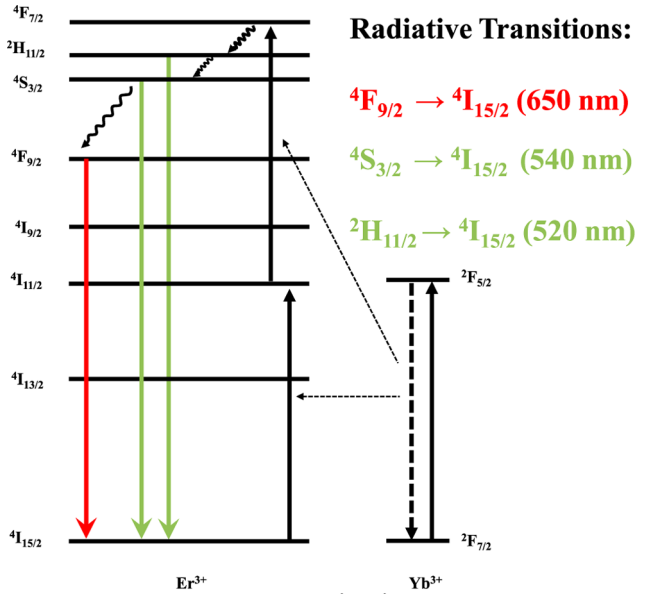

Figure 1. Schematic diagram of the Yb^{3+}–Er^{3+} upconversion mechanism illustrating both radiative and nonradiative (wavy lines) energy transitions.

the radiation-free, whole-body, deep-tissue imaging capability of MRI with the sensitivity of fluorescence detection. Iron oxide nanoparticles have been utilized in many such studies in combination with fluorescent probes such as quantum dots,[13] fluorophores,[14] and even upconverting nanoparticles.[15] One drawback of incorporating iron oxide nanoparticles alongside fluorescent probes is their unfavorable optical properties, which include strong absorption in the UV region extending through the visible spectrum. Such broad band absorption is due to the Fe–O metal–ligand charge-transfer band, Fe–Fe magnetically coupled pair excitations, and Fe^{3+} and Fe^{2+} crystal field transitions.[16] This strong absorption results in the undesirable quenching of the fluorescent emission.[17,18] By contrast, iron oxide nanoparticles exhibit comparatively weak absorption in the near-infrared region, enabling NIR wavelengths (980 nm) to be utilized as an effective means of excitation for upconverting nanomaterials in the presence of iron oxide.

In this Article, we examine the solid-state upconversion emission of $NaYF_4$:Yb,Er nanoparticles in the presence of iron oxide nanoparticles. By combining varying quantities of ~6 nm Fe_3O_4 nanoparticles with either ~10 or ~50 nm $NaYF_4$:Yb,Er nanoparticles, we demonstrate a power-dependent emission. We correlate this emission to iron oxide-induced thermal effects in the mixture that give rise to dominant nonradiative decay in the $NaYF_4$:Yb,Er nanoparticles. The thermal effects reported here should be taken into account in the design of luminescent upconverting hybrid materials.

RESULTS AND DISCUSSION

Upconverting $NaYF_4$:Yb,Er nanoparticles (~10 and ~50 nm) and magnetite nanoparticles were synthesized using previously described methods (Experimental Section).[19,20] The resultant magnetic and upconverting particles were analyzed by transmission electron microscopy (Figure 2). The magnetite nanoparticles (Figure 2a) had an average size of 5.7 ± 1.3 nm, and the $NaYF_4$:Yb,Er nanoparticles had average sizes of 9.2 ± 1.2 and 49.5 ± 6.0 nm (Figure 2b,c). For simplicity, these two samples will be referred to as the 10 nm and 50 nm

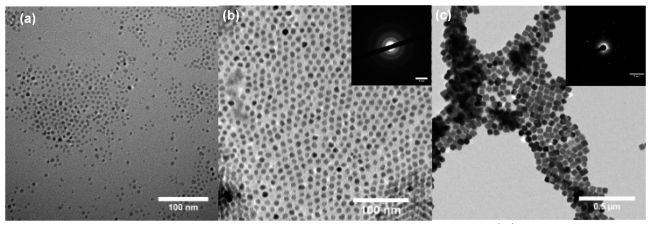

Figure 2. TEM images of the synthesized nanoparticles. Fe_3O_4 (a), 10 nm $NaYF_4$:Yb,Er (b), and 50 nm $NaYF_4$:Yb,Er (c). The insets show selected area electron diffraction patterns (inset scale bars = 5 nm).

samples, respectively. Electron diffraction analyses revealed that the 10 nm upconverting nanocrystals are cubic phase, α-$NaYF_4$:Yb,Er, and the 50 nm upconverting nanocrystals are hexagonal β-$NaYF_4$:Yb,Er (the Figure 2b,c inset shows selected area electron diffraction patterns). Both 10 nm $NaYF_4$ and 50 nm $NaYF_4$:Yb,Er were mixed with varying quantities of iron oxide by the addition of increasing volumes of iron oxide solutions in chloroform. The resulting solutions of chloroform were dried by evaporation onto glass slides for the analysis of their emission properties. The molar ratio of iron to sodium (n(Fe)/n(Na)) was used to determine the relative proportions of the upconverting particles to iron oxide present in the samples. For the 10 nm NaYF4:Yb,Er particles, the n(Fe)/n(Na) ratios studied were 0.000, 0.063 ± 0.001, 0.188 ± 0.004, and 0.285 ± 0.007, and for the 50 nm NaYF4:Yb,Er particles, the n(Fe)/n(Na) ratios studied were 0.000, 0.365 ± 0.009, 0.731 ± 0.017, and 0.830 ± 0.019.

The upconversion spectra of the samples were measured with an optical set up incorporating a 980 nm laser diode, from which the light was focused onto the sample using an objective lens (Figure S2).

The emitted upconversion luminescence was collected using the same objective lens and directed to a spectrometer via a dichroic beam splitter (edge wavelength 900 nm) and a band-pass filter for blocking any returning excitation light (transmission range = 315–710 nm).

The peak wavelength of the laser diode is 974.5 nm. The excitation power was adjusted by altering the current supplied to the laser diode (20–100 mA), and the temperature of the laser diode was held at 25 °C via the integrated thermoelectric cooler. Measurements of the power output of the laser confirm that above threshold its output power is linearly proportional to the input current (Figure S3, Table S1).

Figure 3 illustrates the power-dependent emission in the absence or presence of iron oxide for both particle sizes. (Additional spectra illustrating the power-dependent emission for each n(Fe)/n(Na) value are shown in Figures S4–S11.) We observed a significant decrease in the overall intensity of both emissions in the presence of iron oxide nanoparticles. Furthermore, we observed a greater quenching of the green Er^{3+} emission ($^2H_{11/2}$ and $^4S_{3/2} \rightarrow {}^4I_{15/2}$) relative to the red Er^{3+} emission ($^4F_{9/2} \rightarrow {}^4I_{15/2}$). This greater quenching can be attributed to the shape of the absorption spectrum of the iron oxide nanoparticles (Figure S12), which shows stronger absorption at 550 nm than at 650 nm. Interestingly, we observed that in the presence of iron oxide as the laser power increased both the red and green emission peak intensities increased and then decreased (Figure 3c,d). This process occurred at lower laser powers and iron oxide contents for the 10 nm particles than it did for the mixtures containing 50 nm particles. In this particular example (Figure 3), the onset of the

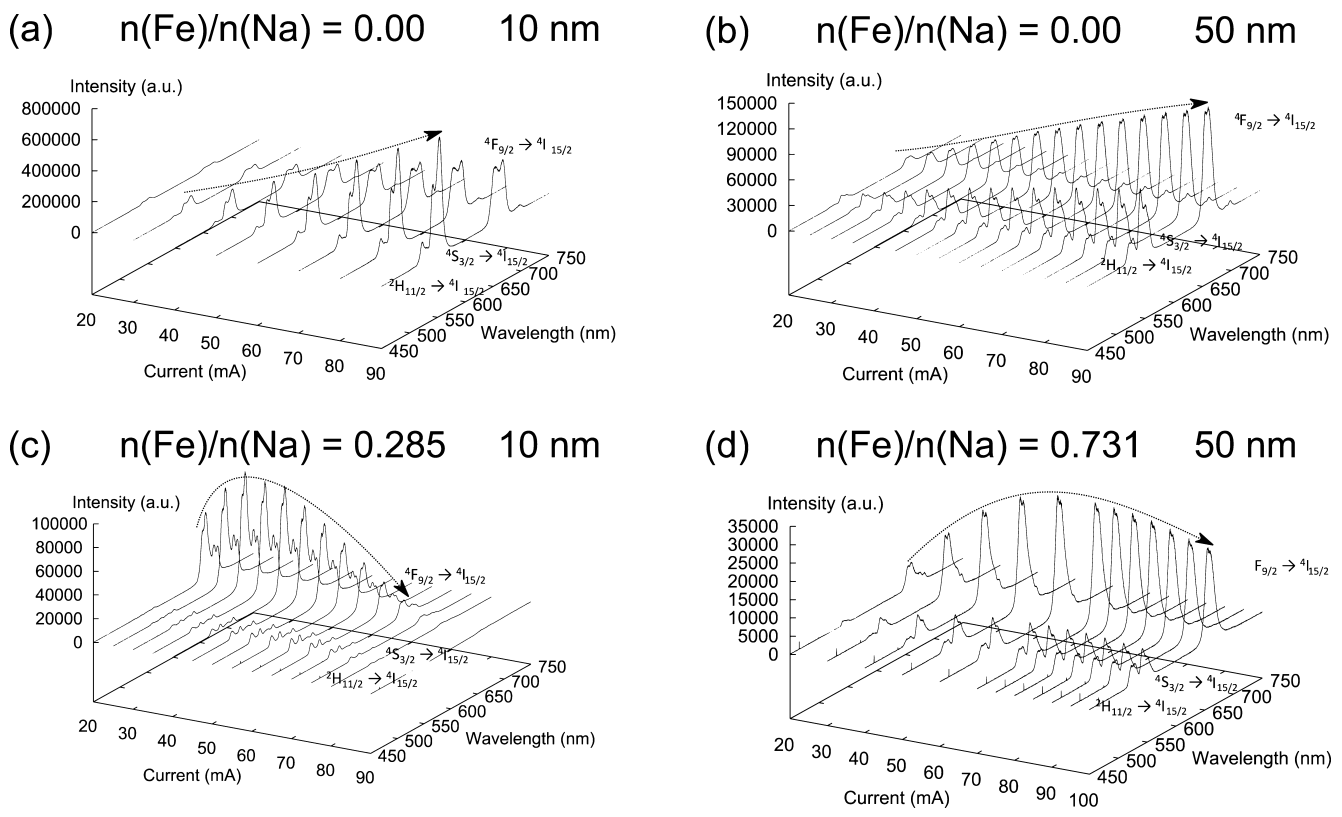

Figure 3. Laser power-dependent emission from 10 nm $NaYF_4$ (a,c) and 50 nm $NaYF_4$ (b,d) in the absence and presence of iron oxide nanoparticles. Emission in the presence of high iron/sodium ratios shows an intensity decrease with increasing laser power.

decrease in red emissions occurs at 30 mA (1890 W/mm^2) for the 10 nm particles (n(Fe)/n(Na) = 0.285) and 60 mA (4780 W/mm^2) for the 50 nm particles (n(Fe)/n(Na) = 0.731).

The power dependence of the erbium emission is shown in the log–log plots of current versus emission peak intensity (Figure S1). The slope of the plots in the absence of iron oxide show a typical two-photon power dependence for both particle sizes (Figure S1a,b).[1] In the presence of iron oxide, the slope of both the red (Figure S1c,d) and green (Figure S1e,f) emission curves decreases with increasing laser current. It was observed that as the iron content is increased the decrease in slope becomes more pronounced. The slope continues to decrease until the gradient of the log–log plot becomes negative (decreasing emission intensity). The point of decreasing emission intensity occurs at correspondingly lower pump currents in the samples with more iron oxide. The 10 nm $NaYF_4$ particles appear to be more susceptible to this decreasing emission intensity than the 50 nm particles because the first onset observed occurred at a current of 40 mA for an n(Fe)/n(Na) = 0.188, whereas the 50 nm particles exhibited this onset only at 80 mA for n(Fe)/n(Na) = 0.365 (i.e., at double the input current and n(Fe)/n(Na)).

We conclude that the observed onset of the decrease at high pump currents is directly related to the n(Fe)/n(Na) ratios and that different sizes of upconverting NaYF4 respond to different degrees in the presence of iron oxide.

It was further observed that the presence of iron oxide caused a significant alteration in the relative intensity ratio of the two transitions, $^2H_{11/2} \rightarrow {}^4I_{15/2}$ (522 nm) and $^4S_{3/2} \rightarrow {}^4I_{15/2}$ (540 nm). The spectra in the absence of iron oxide (Figure 4a,b) show a low relative intensity of the $^2H_{11/2} \rightarrow {}^4I_{15/2}$ peak for both 10 nm NaYF4 and 50 nm NaYF4, respectively. In the presence of iron oxide (Figure 4c,d), however, there is a noticeable increase in the relative intensity of the $^2H_{11/2} \rightarrow {}^4I_{15/2}$ peak.

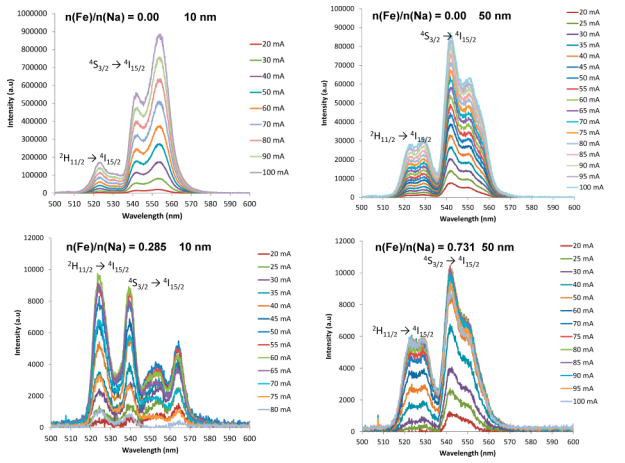

Figure 4. Laser power-dependent spectra showing the $^2H_{11/2} \rightarrow {}^4I_{15/2}$ and $^4S_{3/2} \rightarrow {}^4I_{15/2}$ emissions in the absence of iron oxide (a,b) and in the presence of iron oxide (c,d) for both 10 and 50 nm NaYF4, respectively.

It is known that alterations of the ratios of these two emissions indicate different lattice temperatures.[21−25] We postulate that the iron oxide was heated by the incident laser radiation and this heat was transferred to the upconverting particles. The upconverting $NaYF_4$ particles, excited by the same laser radiation, acted as a sensor to this temperature change.

dx.doi.org/10.1021/am401837h | ACS Appl. Mater. Interfaces 2013, 5, 7875−7880

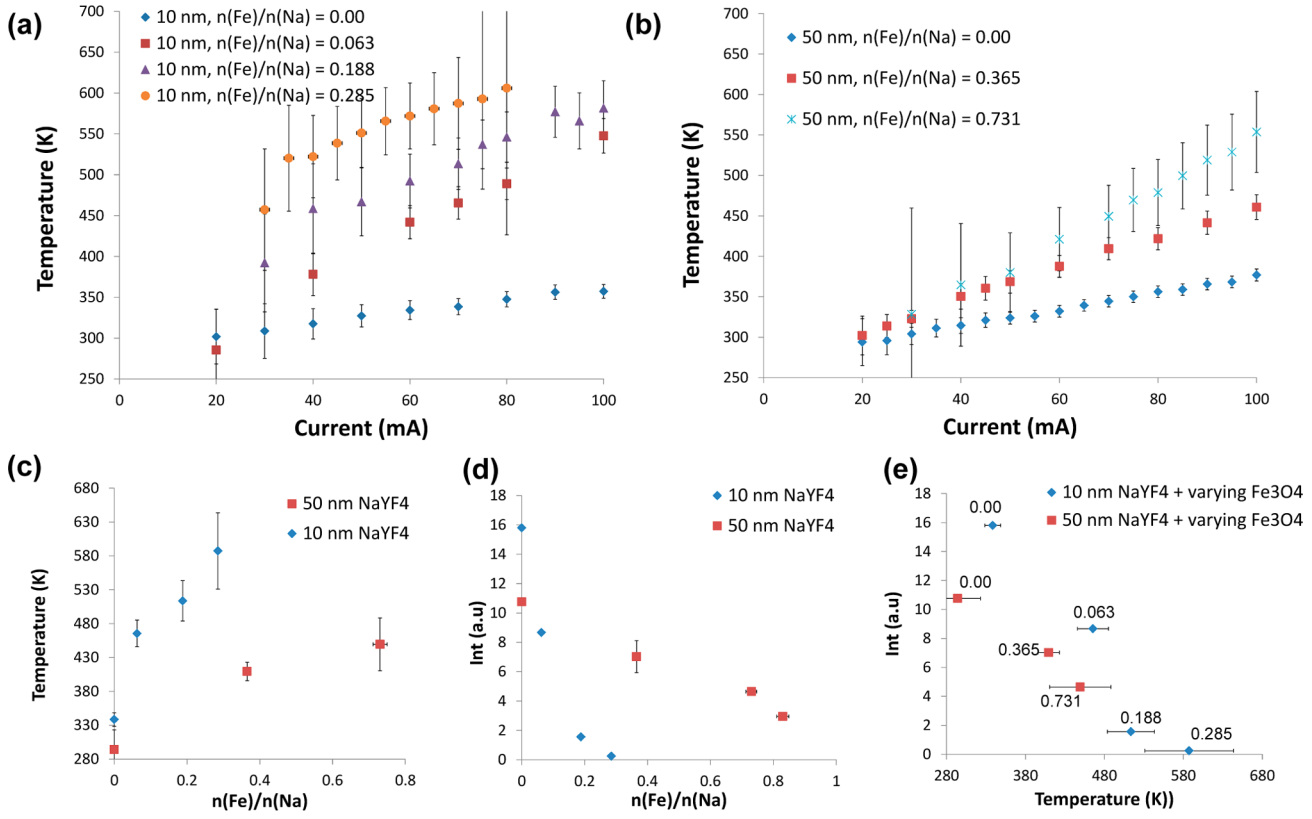

Figure 5. Plots of the calculated $NaYF_4$ lattice temperature with varying laser current and iron oxide content for both 10 nm $NaYF_4$ (a) and 50 nm $NaYF_4$ (b). For a fixed laser current of 70 mA, n(Fe)/n(Na), temperature (K), and the relative peak intensity (Int) can be related (c–e).

The lattice temperature was determined by comparing the relative peak intensity ratios (R_{HS}) of the $^4S_{3/2} \rightarrow {}^4I_{15/2}$ (541 nm) and $^2H_{11/2} \rightarrow {}^4I_{15/2}$ (522 nm) transitions. The $^2H_{11/2} \rightarrow {}^4S_{3/2}$ relaxation is a low-energy-gap transition (Figure 1). As the lattice temperature increases, the $^2H_{11/2}$ level may be thermally repopulated given that the electron energies follow a Boltzmann distribution, implying a finite transition probability of the $^2H_{11/2} \rightarrow {}^4I_{15/2}$ emission.[7] As the temperature is increased, this transition becomes more probable, and the ratio of the intensities of the two peaks R_{HS} is altered to reflect this. The addition of iron oxide to both small and large upconverting particles in the presence of high-intensity laser radiation has a significant effect on the relative intensity ratios of these two transitions (Figure 4). The relative intensities of the two peaks can be related to the temperature of the $NaYF_4$ lattice through the following equation, where ΔE is the energy gap, T is the temperature (K), and R_{HS} is the relative intensity ratio of the $^4S_{3/2} \rightarrow$ and $^4I_{15/2}$ and $^2H_{11/2} \rightarrow {}^4I_{15/2}$ transitions.

$$R_{HS} = R_{HS}(0)\, e^{-\Delta E/k_B T} \quad (1)$$

By rearranging (eq 1) and assuming that the $NaYF_4$ lattice is at room temperature (293 K) for a low laser excitation intensity (20 mA current, ~928 W/mm^2), $R_{HS}(0)$ may be calculated and the lattice temperature may be approximated by

$$T(R_{HS}) = \frac{-\Delta E}{k_B \ln\left(\frac{R_{HS}}{R_{HS}(0)}\right)} \quad (2)$$

The energy gap (ΔE) between the two peaks used is ~637 cm^{-1}. It is noteworthy that iron oxide absorbs NIR light at 980 nm owing to the edge of the intervalence charge-transfer band present between neighboring 3d t_{2g} electrons on octahedral sites resulting from the Fe^{2+} ions in magnetite.[26−28] This absorption band is centered at approximately 0.6 eV (~2066 nm) and extends to ~1.4 eV (~885 nm).[28] The calculated maximum temperatures for $NaYF_4$ in the absence of iron oxide nanoparticles are 357 and 376 K for 50 and 10 nm $NaYF_4$:Yb,Er at 100 mA laser current, respectively. With increasing quantities of iron oxide, increasingly higher temperatures were measured (up to 606 and 553 K for 10 and 50 nm $NaYF_4$:Yb,Er, respectively), with a consequent measurable effect on the erbium emissions. Most importantly, the 50 and 10 nm $NaYF_4$:Yb,Er particles displayed different temperature sensitivities (Figure 5a,b), as the onset of the decrease in emission occurred at lower laser powers for the smaller $NaYF_4$:Yb,Er particles. R_{HS} alterations appeared to be more significant in the 10 nm particles than in 50 nm particles, providing further evidence of a higher lattice temperature in 10 nm $NaYF_4$:Yb,Er. This difference can be attributed to the ~5 times greater surface area to volume ratio of the 10 nm particles compared with that of the 50 nm particles, conferring greater sensitivity to the local iron oxide presence. The smaller size of the crystals and the different crystal structures (cubic vs hexagonal) can provide additional nonradiative pathways that enhance the multiphonon relaxation rates.[7]

The relative peak intensity, temperature, and n(Fe)/n(Na) ratios are related (Figure 5c,d,e) at a fixed high excitation current of 70 mA (5.74 kW/mm^2). It can be seen that at this laser power there is a trend of increasing temperature with iron content, decreasing relative peak intensity with iron content, and decreasing relative peak intensity with increasing lattice temperature (all intensities have been normalized to the minimum measurement at 20 mA).

The changes observed in the power-dependent upconversion spectra (Figures 3 and S1) are related to changes in the $NaYF_4$ lattice temperature (Figure 5). The increasing thermal energy within the upconverting nanocrystals promoted multiphonon relaxation processes, resulting in depopulation of the excited $^4S_{3/2}$, $^2H_{11/2}$, and $^4F_{9/2}$ states. This reduced the radiative transition probability of these states and subsequently caused a decrease in the emission intensity with increasing laser power (Figure 3). Most importantly, this behavior was not present in the absence of iron oxide nanoparticles over the measured range of laser powers. It was demonstrated that $NaYF_4$ lattice heating increased with both laser power and iron oxide content. The results herein are consistent with a model of laser-induced heating of Fe_3O_4 resulting in a subsequent energy transfer that was detected optically by the upconverting component of the mixture.

CONCLUSIONS

We have demonstrated that in the presence of iron oxide nanoparticles the emission from upconverting nanoparticles is power dependent. This power dependence is related to the changes in the $NaYF_4$:Yb,Er lattice temperature that in turn is due to a laser-induced heating of the Fe_3O_4 particles and a subsequent transfer of thermal energy to the upconverting $NaYF_4$:Yb,Er particles. These temperature changes can be monitored by careful observation of the $^2H_{11/2}$ and $^4S_{3/2} \rightarrow {}^4I_{15/2}$ transitions. The two different nanoparticle sizes (10 and 50 nm) exhibited different power dependencies and sensitivity to the local iron oxide content. The findings highlight an important concept to be taken into consideration when designing novel upconverting hybrid materials. This study shows that the laser-induced thermal behavior of nonupconverting constituents can play an important role in dictating the upconverting properties of the nanoparticles.

EXPERIMENTAL SECTION

Magnetite nanoparticles were synthesized by using the thermal decomposition method established by Sun et al.[19] Briefly, 1 mmol of $Fe(acac)_3$, 5 mmol of tetradecanediol, 3 mmol of oleic acid, and 3 mmol of oleylamine were dissolved in dibenzyl ether. The organic phase was heated in the presence of N_2 gas to 100 °C for 30 min, 200 °C for 2 h, and refluxed at 300 °C for 1 h. The product was precipitated and washed with ethanol 3 times by centrifugation at 4000 rpm.

Upconverting $NaYF_4$:Yb,Er was synthesized using the method described by Boyer et al.[20] Two millimoles of sodium trifluoroacetate, 1.56 mmol of yttrium trifluoroacetate, 0.4 mmol of ytterbium trifluoroacetate, 0.04 mmol of erbium trifluoroacetate, 10 mmol of oleic acid, and 10 mmol of oleylamine were mixed in 20 mmol of 1-octadecene. The organic mixture was degassed at 100 °C for 30 min and rapidly heated to 300 °C under N_2 gas. The product was washed with ethanol in a similar manner and yielded a white solid pellet of the 10 nm $NaYF_4$ nanoparticles. The larger 50 nm $NaYF_4$:Yb,Er nanoparticles were synthesized by taking 1 mmol of product from the initial reaction and rapidly heating it to 330 °C in the presence of 1.3 mmol of sodium trifluoroacetate, 10 mmol of oleic acid, and 10 mmol of oleylamine dissolved in 20 mmol of 1-octadecene.

ASSOCIATED CONTENT

Supporting Information

Experimental details, double-logarithmic plots, optical set up, laser-power dependency characteristics, power-dependent upconversion spectra for 10 and 50 nm nanoparticles with varying n(Fe)/n(Na) ratios, and iron oxide absorption spectrum. This material is available free of charge via the Internet at http://pubs.acs.org.

AUTHOR INFORMATION

Corresponding Author

*E-mail:swaminatha.iyer@uwa.edu.au.

Author Contributions

The manuscript was written through contributions of all authors. All authors have given approval to the final version of the manuscript.

Notes

The Authors declare no competing financial interest.

ACKNOWLEDGMENTS

The authors acknowledge the facilities and the scientific and technical assistance of the Australian Microscopy & Microanalysis Research Facility at the Centre for Microscopy, Characterisation & Analysis, The University of Western Australia, which is a facility funded by the University, State, and Commonwealth Governments. We thank Dr. Xiaoyong Huang and Prof. Xiaogang Liu of the Department of Chemistry, National University of Singapore, for their input in this study. Michael Challenor acknowledges the Graduate Research School of The University of Western Australia for funding in the form of a University Postgraduate Award (UPA) Scholarship. Peijun Gong is supported by The University of Western Australia and the China Scholarship Council. The authors acknowledge funding from the Australian Research Council.

REFERENCES

(1) Haase, M.; Schäfer, H. *Angew. Chem., Int. Ed.* **2011**, *50*, 5808.
(2) Teng, X.; Zhu, Y.; Wei, W.; Wang, S.; Huang, J.; Naccache, R.; Hu, W.; Tok, A. I. Y.; Han, Y.; Zhang, Q.; Fan, Q.; Huang, W.; Capobianco, J. A.; Huang, L. *J. Am. Chem. Soc.* **2012**, *134*, 8340.
(3) Wang, F.; Han, Y.; Lim, C. S.; Lu, Y.; Wang, J.; Xu, J.; Chen, H.; Zhang, C.; Hong, M.; Liu, X. *Nature* **2010**, *463*, 1061.
(4) Wang, F.; Liu, X. *Chem. Soc. Rev.* **2009**, *38*, 976.
(5) Auzel, F. *Chem. Rev.* **2004**, *104*, 139.
(6) Li, A. H.; Lü, Q. *Europhys. Lett.* **2011**, *96*, 18001.
(7) Keyue, W.; Jingbiao, C.; Xiangxing, K.; Yunjun, W. *J. Appl. Phys.* **2011**, *110*, 053510.
(8) Vetrone, F.; Naccache, R.; Zamarrón, A.; Juarranz de la Fuente, A.; Sanz-Rodríguez, F.; Martinez Maestro, L.; Martín Rodriguez, E.; Jaque, D.; García Solé, J.; Capobianco, J. *ACS Nano* **2010**, *4*, 3254.
(9) Shan, J.; Kong, W.; Wei, R.; Yao, N.; Ju, Y. *J. Appl. Phys.* **2010**, *107*, 054901.
(10) Su, Q.; Han, S.; Xie, X.; Zhu, H.; Chen, H.; Chen, C.-K.; Liu, R.-S.; Chen, X.; Wang, F.; Liu, X. *J. Am. Chem. Soc.* **2012**, *134*, 20849.
(11) Su, L. T.; Karuturi, S. K.; Luo, J.; Liu, L.; Liu, X.; Guo, J.; Sum, T. C.; Deng, R.; Fan, H. J.; Liu, X.; Tok, A. I. Y. *Adv. Mater.* **2013**, *25*, 1603.
(12) Liang, C.; Chao, W.; Xinxing, M.; Qinglong, W.; Yao, C.; Han, W.; Yonggang, L.; Zhuang, L. *Adv. Funct. Mater.* **2013**, *23*, 272.
(13) Koole, R.; Mulder, W. J. M.; van Schooneveld, M. M.; Strijkers, G. J.; Meijerink, A.; Nicolay, K. *Wiley Interdiscip. Rev.: Nanomed. Nanobiotechnol.* **2009**, *1*, 475.
(14) Evans, C. W.; Latter, M. J.; Ho, D.; Peerzade, S. A. M. A.; Clemons, T. D.; Fitzgerald, M.; Dunlop, S. A.; Iyer, K. S. *New J. Chem.* **2012**, *36*, 1457.
(15) Gai, S. L.; Yang, P. P.; Li, C. X.; Wang, W. X.; Dai, Y. L.; Niu, N.; Lin, J. *Adv. Funct. Mater.* **2010**, *20*, 1166.
(16) He, Y. P.; Miao, Y. M.; Li, C. R.; Wang, S. Q.; Cao, L.; Xie, S. S.; Yang, G. Z.; Zou, B. S.; Burda, C. *Phys. Rev. B* **2005**, *71*, 125411.

(17) Feng, C.; Wenbo, B.; Lingxia, Z.; Yuchi, F.; Jianlin, S. *J. Mater. Chem.* **2011**, *21*, 7990.
(18) Chen, F.; Zhang, S.; Bu, W.; Liu, X.; Chen, Y.; He, Q.; Zhu, M.; Zhang, L.; Zhou, L.; Peng, W.; Shi, J. *Chem.—Eur. J.* **2010**, *16*, 11254.
(19) Sun, S.; Zeng, H.; Robinson, D.; Raoux, S.; Rice, P.; Wang, S.; Li, G. *J. Am. Chem. Soc.* **2004**, *126*, 273.
(20) Boyer, J.-C.; Vetrone, F.; Cuccia, L.; Capobianco, J. *J. Am. Chem. Soc.* **2006**, *128*, 7444.
(21) Liu, W.; Sun, J.; Li, X.; Zhang, J.; Tian, Y.; Fu, S.; Zhong, H.; Liu, T.; Cheng, L.; Zhong, H.; Xia, H.; Dong, B.; Hua, R.; Zhang, X.; Chen, B. *Opt. Mater.* **2013**, *35*, 1487.
(22) Li, A. H.; Sun, Z. J.; Lü, Q. *J. Nanopart. Res.* **2012**, *15*, 1.
(23) Mao, Y.; Tran, T.; Guo, X.; Huang, J. Y.; Shih, C. K.; Wang, K. L.; Chang, J. P. *Adv. Funct. Mater.* **2009**, *19*, 748.
(24) Mengistie, L. D.; Duarte, A.; Isabel, P. S.; Luis, M. L. M.; Rocha, J.; Luís, D. C. *Adv. Mater.* 2013, DOI: 10.1002/adma.201300892.
(25) Jaque, D.; Vetrone, F. *Nanoscale* **2012**, *4*, 4301.
(26) Fontijn, W. F. J.; van der Zaag, P. J.; Feiner, L. F.; Metselaar, R.; Devillers, M. A. C. *J. Appl. Phys.* **1999**, *85*, 5100.
(27) Tang, J.; Myers, M.; Bosnick, K. A.; Brus, L. E. *J. Phys. Chem. B* **2003**, *107*, 7501.
(28) Park, S. K.; Ishikawa, T.; Tokura, Y. *Phys. Rev. B* **1998**, *58*, 3717.